Supplementary information:

Overcoming the Thermo-Refractive Noise Limit for a Full-Spectrum Hertz-Linewidth Microcomb

Chao Zhou[1,†], Runlin Miao[2,†,*], Pan Han[3], Mingxin Yang[3], Xing Zou[3], Ke Wei[4,5*], Ke Yin[3*], Tian Jiang[3,4,5*]

[1]College of Computer Science and Technology, National University of Defense Technology, Changsha, China
[2]National Innovation Institute of Defense Technology, Academy of Military Sciences PLA China, Beijing, China
[3]College of Advanced Interdisciplinary Studies, National University of Defense Technology, Changsha, China
[4]College of Science, National University of Defense Technology, Changsha, China
[5]Hunan Research Center of the Basic Discipline for Physical States, National University of Defense Technology, Changsha, China
[†]These authors contributed equally: Chao Zhou, Runlin Miao.
*Email: mrl1123@126.com, weikeaep@163.com, yin@nudt.edu.cn, tjiang@nudt.edu.cn

This Supplementary Information consists of the following sections:

Supplementary Note 1: Characterization of the DFB laser

The characteristics of the high-power distributed-feedback (DFB) laser used in our experiments are summarized in Supplementary Figure 1. At a drive current of 600 mA, the DFB laser emits an output power exceeding 150 mW, with a threshold current of approximately 50 mA. At a stabilized temperature of 25℃, the emission wavelength can be tuned over a range of 1 nm from an initial wavelength of 1548.692 nm by adjusting the drive current within a 500-mA range.

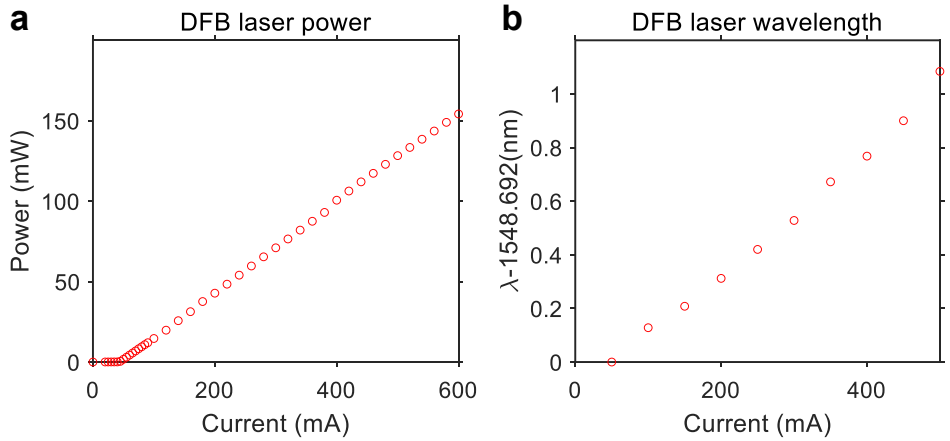

Supplementary Figure 1. Characteristics of the DFB laser. a, Output power as a function of drive current. At 600 mA, the output exceeds 150 mW. **b,** Emission wavelength versus drive current, showing a tuning range of 1 nm around 1548.692 nm at 25 ℃.

Supplementary Note 2. Characterization of the microresonator

A typical resonance transmission spectrum of the TE_{00} mode for an add-drop microresonator under critical coupling is shown in Supplementary Figure 2a. A Lorentzian fit yields a total cavity decay rate of $\kappa = 2\pi \times 32.8$MHz, corresponding to a loaded quality factor (Q_L) of 5.46×10^6 and an intrinsic quality factor (Q_0) of approximately 1.09×10^7. A high Q factor is critical for microcomb generation, as the power threshold P_{th} for Kerr parametric oscillation scales as: $P_{th} \propto 1/(D_1 {Q_L}^2)$, where the free spectral range (FSR) $D_1 = 2\pi \times 100.7$ GHz. The estimated P_{th} of 1.6 mW is sufficiently low to facilitate coherent SIL microcomb generation. The measured and fitted integrated dispersion dispersion ($D_{int}/2\pi$) is presented in Supplementary Figure 2b. The group velocity dispersion (GVD) at the pump wavelength is $D_2/2\pi = 0.36$ MHz, confirming the anomalous dispersion required for bright soliton formation.

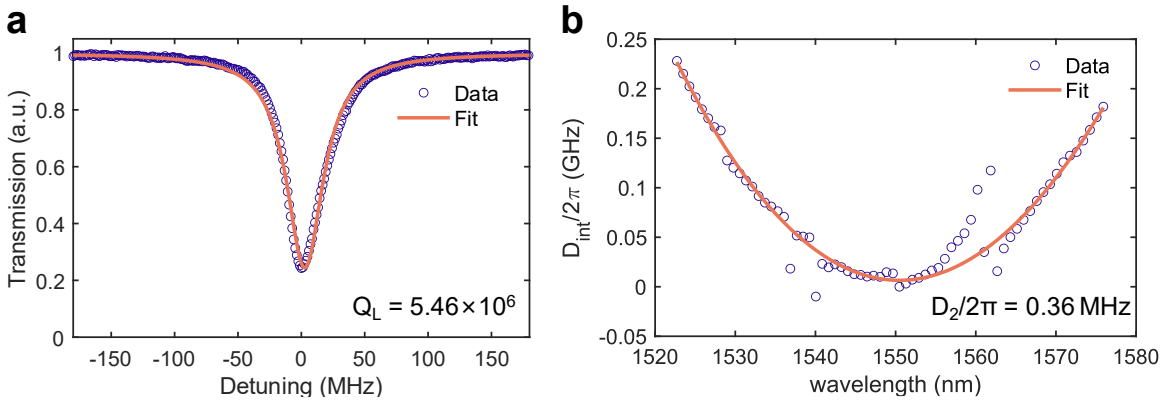

Supplementary Figure 2. Characterization of the Si_3N_4 microresonator. a, Transmission spectrum of a TE_{00} mode under critical coupling. A Lorentzian fit gives a total cavity decay rate of $\kappa = 2\pi \times 32.8$ MHz, corresponding to a loaded quality factor (Q_L) of 5.46×10^6. **b,** Measured (blue circles) and fitted (red line) integrated dispersion $D_{int}/2\pi$. The anomalous GVD at the pump wavelength is $D_2/2\pi$ = 0.36 MHz.

Supplementary Note 3. Self-injection locking to the microresonator and soliton microcomb generation

Self-injection locking (SIL) is a key technique for enhancing the frequency stability and narrowing the linewidth of semiconductor lasers. The underlying principle involves using optical feedback from a high-Q external resonator to lock the laser frequency to one of the cavity's resonant modes. This process can be simulated using coupled rate equations, and the tuning curve of the SIL to a high-Q microresonator can be expressed as[1]:

$$\xi = \zeta + \frac{K}{2} \cdot \frac{2\zeta \cos\psi + (1+\beta^2-\zeta^2)\sin\psi}{(1+\beta^2-\zeta^2)^2+4\zeta^2} \quad \text{(S1)}$$

where ξ denotes the normalized detuning between the system's output frequency and the microresonator's resonance frequency, ζ represents the normalized detuning between the free-running laser frequency and the microresonator's resonance frequency, K is the combined coupling coefficient of the system, reflecting the strength of energy exchange between the laser and the microresonator, $\psi = \psi_0 + \kappa\tau_s\zeta/2$ is the phase delay between the laser cavity and the microresonator including the initial phase ψ_0, the round-trip time of the optical feedback τ_s, and the total cavity decay rate κ. The parameter β denotes the mode splitting of the microcavity originating from intracavity backscattering. The parameters ξ, ζ and β are normalized by $\kappa/2$. Experimentally, $\kappa = \kappa_0 + \kappa_{ex}$ is measured as $2\pi \times 32.8$ MHz, with equal intrinsic loss κ_0 and external coupling rate κ_{ex} of $2\pi \times 16.4$MHz.

Applying K = 40, ψ = 0π and β = 0.5 to Eq. S1, the resulting tuning curve is shown in Supplementary Figure 3. The black dashed line denotes the linear tuning curve of the free-running laser, while the blue solid curve corresponds to the tuning curve under SIL.

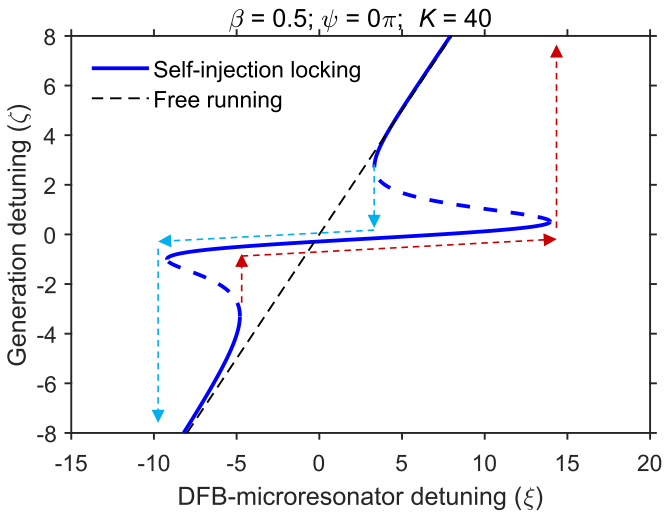

Supplementary Figure 3. Simulated tuning curves for self-injection locking (SIL). The blue solid curve shows the SIL tuning behavior, while the black dashed line represents the free-running laser.

When in the SIL&pump-OIL configuration, the total optical feedback into the DFB laser originates from two distinct backscattering contributions:

1. Direct backscattering of the original pump light from the microresonator's Rayleigh scattering, described by the intrinsic complex reflection coefficient Γ(ω).

2. Another backscattering arising when a fraction of pump light at the microresonator output is collected and then reinjected into the microresonator. This reinjected field undergoes the same Rayleigh backscattering process, thereby producing a second backscattered field that is a delayed, amplitude scaled, and phase shifted replica of the first. It can be modeled as a frequency independent complex factor $\Gamma(\omega)\times R e^{i\Phi}$, where $0 \le R \le 1$ is the amplitude ratio of the reinjected laser to the direct pump laser, and Φ is the extra phase accumulated along the external path.

Following the method reported in Supplementary Ref. 2, we quantitatively analyze the feedback behavior of dual backward scattering. The total effective backscattering coefficient can be described as:

$$\Gamma_{\text{eff}}(\omega) = \Gamma(\omega)\left(1 + R\,e^{i\Phi}\right) \tag{S2}$$

Its amplitude and phase can be expressed as:

$$\left|\Gamma_{\text{eff}}\right| = \left|\Gamma\right|\sqrt{1 + R^2 + 2R\cos\Phi} \tag{S3}$$

$$\arg\left(\Gamma_{\text{eff}}\right) = \arg\left(\Gamma\right) + \arg\left(1 + R\,e^{i\Phi}\right) = \psi + \varphi \tag{S4}$$

Where $\varphi = arctan\left(\frac{R\,sin\,\Phi}{1+R\,cos\,\Phi}\right)$ and ψ is the phase of the direct pump laser backscattered field. Considering the new effective backscattering coefficients in Equations (S3) and (S4), similar to Equation (S1), the newly modified dual-source locking curve equation can be derived as follows:

$$\xi = \zeta + \frac{K\sqrt{1+R^2+2R\cos\Phi}}{2} \cdot \frac{2\zeta\cos(\psi+\varphi)+(1+\beta^2-\zeta^2)\sin(\psi+\varphi)}{(1+\beta^2-\zeta^2)^2+4\zeta^2} \tag{S5}$$

This formula directly presents the influence of two core control parameters, the amplitude ratio and phase of the external feedback loop, on the behavior of injection locking. The coupling coefficient K is scaled by a factor of $\sqrt{1+R^2+2R\cos\Phi}$ and can vary between the set upper and lower bounds of $K(1-R)$ and $K(1+R)$, respectively, which directly adjusts the locking bandwidth of the system. The additional phase φ also shapes the profile of the locking curve. When $R = 0$, this formula fully degenerates into Equation (S1).

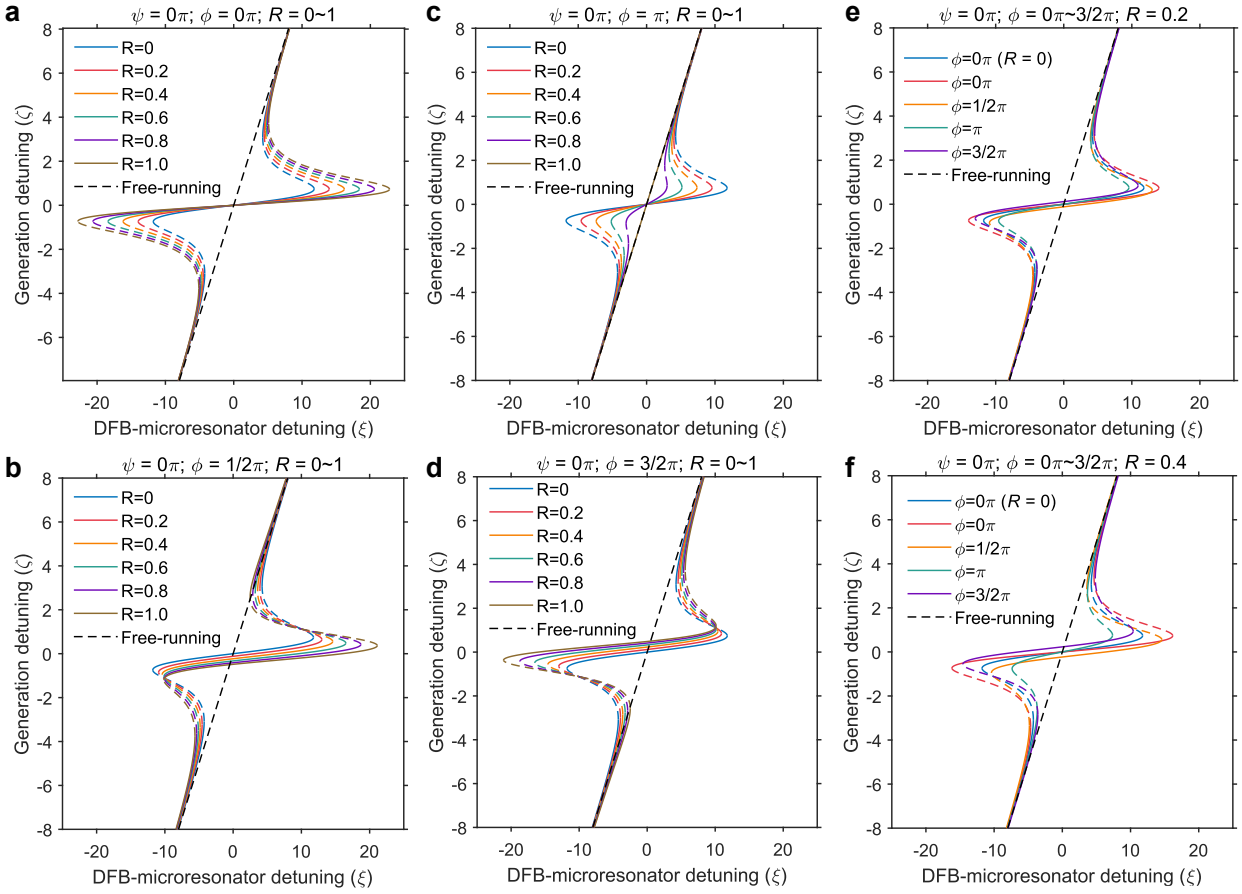

Supplementary Figure 4. Simulated tuning curves for SIL&pump-OIL. a–d correspond to different extra feedback phases accumulated along the external path of Φ = 0, 0.5π, π, and 1.5π, respectively. The phase of direct backscattering of the original pump light ψ is set to 0. The feedback amplitude coefficient R increases from 0 to 1.0 with a step value of 0.2. e-f correspond to different feedback amplitude coefficient R of 0.2 and 0.4, respectively. Extra feedback phases Φ change from 0π to 1.5π with a step value of 0.5π. When R=0, the tuned curvature of SIL&pump-OIL agrees well with the result obtained with SIL only (blue curve). The black dashed line represents the free-running laser.

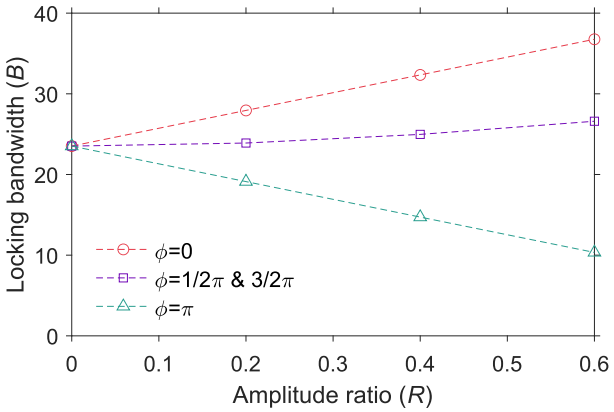

Supplementary Figure 5. Dependence of injection locking bandwidth (*B*) on amplitude ratio (*R*) and extra feedback phase (Φ).

As shown in Supplementary Figure 4, we quantitatively analyze the two contributions to the tuning curvature of injection locking under the SIL&pump-OIL configuration. Under different extra feedback phases Φ (Supplementary Figure 4a–d), the profile of the curvature changes as the feedback amplitude coefficient R increases. In particular, opposite behaviors are observed at Φ=0 and Φ=π, corresponding to constructive interference and destructive interference, which realize the widening and shrinking of the locking bandwidth, respectively. In addition, when the feedback amplitude coefficient R is fixed (Supplementary Figure 4e–f), different feedback phases deform the symmetry of the curve and would enable laser frequency pulling.

Supplementary Figure 5 summarizes the injection locking bandwidth (B) results for different amplitude ratios R and extra feedback phases Φ of the injected optical field. As the feedback coefficient increases ($R = 0.2, 0.4$ and 0.6), the variation range of the injection locking bandwidth under different feedback phases (Φ=0, 0.5π&1.5π and π) is $\delta B/B = \pm 18.8\%$, $\pm 37.5\%$ and $\pm 56.2\%$, respectively. These results are ideal predictions under linear conditions. However, in the actual experiment, the feedback phase undergoes random fluctuations induced by unavoidable environmental perturbations, leading to a time-averaged response that effectively averages out the phase-sensitive modulation predicted by theory. Consequently, no significant variation in the injection locking range is observed.

Next, we developed a setup to trigger and monitor the SIL soliton microcomb generation in Supplementary Figure 6a. The DFB laser diode is firstly butt-coupled to the microresonator. The laser temperature is stabilized by a control module, and its frequency is tuned via the drive current. In addition to a DC bias, the current can be modulated by an external signal (e.g., a sine, triangular, or square wave). In this work, we used a triangular wave synchronized with the oscilloscope. The generated optical frequency comb from the microresonator's through port is split into three paths: one to an optical spectrum analyzer (OSA) for spectral monitoring, one directly to a photodetector (PD), and one through a fiber Bragg grating (FBG) to filter out the high-power pump light before being detected by another PD. The PD signals are displayed on an oscilloscope to observe power evolution. By sweeping the pump laser frequency across a cavity resonance while applying an

optimal feedback phase, the SIL soliton evolution can be monitored. Supplementary Figure 6b shows the experimental power evolution of the pump transmission and the comb power (pump filtered). Distinct SIL and soliton steps are observed at the optimal feedback phase, confirming the generation of the soliton microcomb.

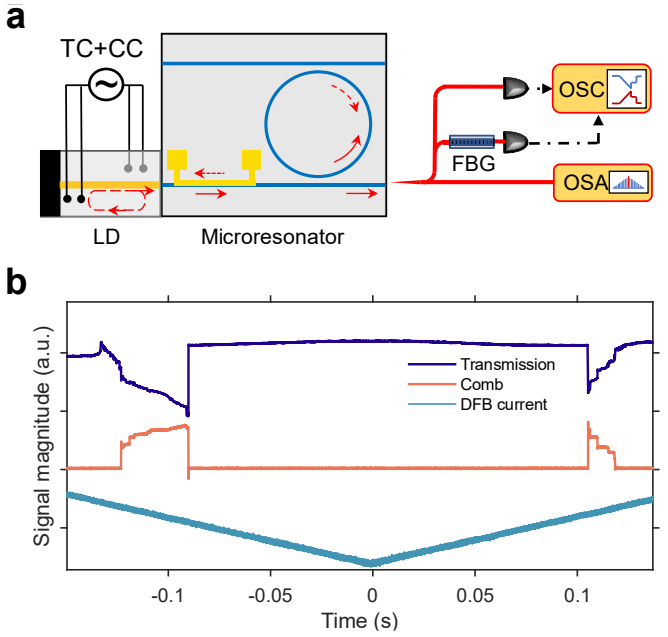

Supplementary Figure 6. Experimental setup for SIL soliton microcomb generation and monitoring. a, Schematic of the setup. LD: laser diode; TC: temperature controller; CC: current controller; FBG: fiber Bragg grating; OSA: optical spectrum analyzer; OSC: oscilloscope. **b,** Power evolution of the pump transmission (blue) and comb power (orange, pump filtered) during a current sweep, showing distinct SIL and soliton steps.

Supplementary Note 4. Experimental setup for cascaded SIL&OIL architecture

Supplementary Figure 7 shows the schematic diagram of the experimental setup for the cascaded SIL&OIL microcomb generation, which comprises three main parts: SIL microcomb generation, a comb feedback oscillator for noise suppression, and a coherence measurement system. First, for SIL microcomb generation, we use an integrated add-drop silicon nitride (Si_3N_4) microresonator with a cross-section of 2.2 μm (width) × 800 nm (height) and a loaded quality factor (Q_L) of 5.46×10^6. The resonator was fabricated via a deep-ultraviolet (DUV) subtractive process on 150-mm-diameter (6-inch) wafers[3]. A commercial distributed-feedback (DFB) laser is butt-coupled to the microresonator via inverse tapers, achieving a coupling efficiency of 56% (2.5 dB insertion loss). The laser temperature is stabilized at 25°C using a thermo-electric cooler (TEC).

Second, for OIL, the output microcomb is amplified to ~100 mW using an erbium-doped fiber amplifier (EDFA). A 10% fraction of the power is monitored by an optical spectrum analyzer (OSA), while the remaining 90% is directed—via a 3-dB coupler—to the feedback oscillator and the coherence measurement system. In the feedback path, a tunable bandpass filter (TBPF) is used to select the target comb line. A second optical amplifier and an electronic variable optical

attenuator (EVOA) regulate the feedback power. The basic total insertion loss of the experimental setup is ~13.46 dB and the loss budget includes: Chip-to-fiber coupling at both input and output facets, providing loss of 2×3.75 dB=7.5 dB, 10% of the light is directed to the OSA for spectral monitoring, giving loss of 0.46 dB, a 3 dB coupler is used for splitting to measurement and feedback arms, introducing loss of 3 dB, and finally, the TBPF also contributes an insertion loss of 2.5 dB. We adopted a fully polarization-maintaining experimental link to minimize polarization drift induced by environmental perturbations (e.g., temperature fluctuations, fiber vibration), which is particularly important for long-term stability during measurements.

Finally, for coherence measurement, the remaining comb light is sent to an unbalanced Mach-Zehnder interferometer (MZI) with a 200-meter fiber delay line for delayed self-heterodyne detection. An acousto-optic modulator (AOM) in the reference arm provides a 40 MHz frequency shift, and a balanced photodetector captures the heterodyne signal for phase noise analysis.

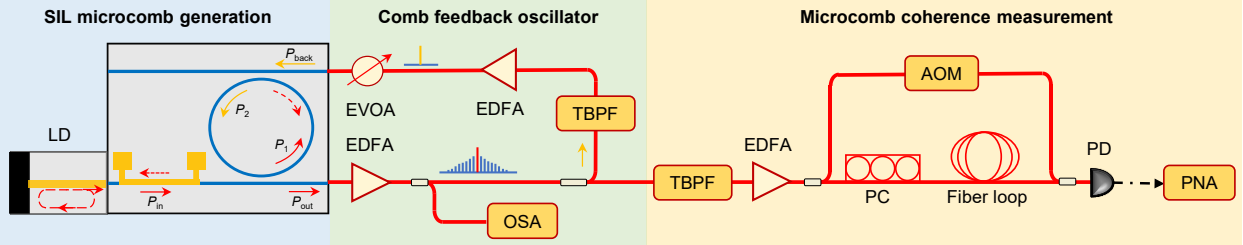

Supplementary Figure 7. Experimental setup for SIL soliton microcomb generation and monitoring. The system includes SIL microcomb generation, an OIL feedback loop for noise suppression, and a delayed self-heterodyne interferometer for coherence measurement. Key components: EDFA, erbium-doped fiber amplifier. OSA, optical spectrum analyser; EVOA, electronic variable optical attenuator; PC, polarization controller; AOM, acoustic optical modulator; PD, photodiode; PNA, phase noise analyser.

We note that the feedback power ratio η is a critical parameter in optical injection locking, as it governs the strength of the reinjected field and determines the noise suppression performance as well as the soliton dynamical regimes (see main text Fig. 4). Here we provide a detailed definition of η and describe its experimental determination. η is defined as the power re-entering the microresonator (P_2) relative to the intracavity comb power (P_1), i.e., $\eta = P_2/P_1$. Since both P_1 and P_2 are intracavity powers and cannot be accessed directly, we determine η experimentally by measuring the on-chip waveguide powers that are proportional to them. As illustrated in Supplementary Figure 7, P_1 is proportional to the on-chip input power P_{in} coupled into the microresonator from the bus waveguide, and P_2 is proportional to the on-chip feedback power P_{back} reinjected from the opposite side. Because the two coupling waveguides are nominally symmetric with respect to the microresonator, the input coupling efficiency η_1 (from bus to cavity) and the feedback coupling efficiency η_2 (from feedback waveguide to cavity) are approximately equal. Thus, $\eta = P_2/P_1 = \eta_2 P_{back}/(\eta_1 P_{in}) \approx P_{back}/P_{in}$.

The determination of P_{back} and P_{in} depends on whether the pump line or a sideband comb line is used for OIL. For the pump line, the measurement is straightforward. P_{in} is obtained by measuring the output power of the DFB laser and accounting for the chip-to-fiber coupling loss at

the input facet. P_{back} is obtained by measuring the output power of the EDFA, subtracting the attenuation set by the EVOA, and then accounting for the fiber-to-chip coupling loss at the feedback input facet. For a sideband comb line, P_{back} is obtained in the same manner. However, P_{in} cannot be measured directly because there is no external input at the sideband frequency. Instead, we deduce P_{in} from the measured on-chip output power P_{out} of that comb line using the well-established input-output relation for a microresonator:

$$P_{\text{out}}/P_{\text{in}} = \kappa_{ex} T_r \frac{F}{\pi} \frac{2\eta}{1+(\delta\omega/(\kappa/2))^2} \tag{S6}$$

Here, κ_{ex} is the coupling rate to the bus waveguide, T_r is the round-trip time in the microcavity, η = 0.25 is the waveguide coupling efficiency of the add-drop microresonator, F is the finesse of the microresonator, κ is the loss of the microresonator, and $\delta\omega$ is the angular frequency detuning of the comb line from the nearest cavity resonance. The detuning $\delta\omega$ for the pump line is known from the modified Lugiato – Lefever equation ($\delta\omega_{\text{p}} = 2.94\,\kappa/2$), and the detuning for a sideband at mode μ is obtained by accounting for the cavity dispersion: $\omega_\mu = \omega_0 + D_1\mu + \frac{D_2}{2}\mu^2 + \cdots$. Using these parameters, we calculate P_{in} and find that, for our device, $P_{\text{in}} \approx P_{\text{out}} + 18.7$ dB.

Supplementary Note 5. Optimal frequency noise performance for different fiber loop lengths

As discussed in the main text, both the fiber loop length and the feedback power ratio (η) are critical for frequency noise suppression. However, increasing the fiber length reduces the frequency spacing of the external cavity modes, which promotes multi-mode competition and lowers the maximum achievable η for stable soliton operation.

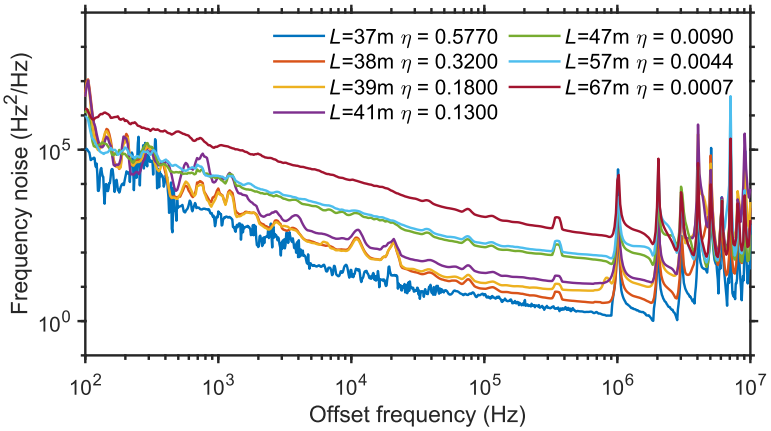

Supplementary Figure 8. Frequency noise performance for different fiber loop lengths. The shortest loop (37 m) achieves the lowest noise, with performance degrading as loop length increases due to reduced maximum stable feedback ratio η.

In this note, we investigate the frequency noise of the SIL & OIL microcomb using fiber loops longer than the 37 m benchmark adopted in the main text (Supplementary Figure 8). The 37 m

length was the shortest fiber loop that could accommodate the discrete EDFA, bandpass filter (BPF), and EVOA. For each tested length, the maximum stable η was recorded. The results show a gradual deterioration in frequency noise with increasing loop length, attributable to a rapid decrease in η. Future studies will explore loops shorter than 37 m when on-chip filters and attenuators are employed, thereby enabling the determination of the optimal feedback loop length.

Note that the frequency noise of SIL&Pump-OIL exists a distinct frequency noise bump below a 1 kHz offset, which may be attributed to the temperature fluctuation and mechanical vibration. Despite the relatively poor long-term stability, this strategy is highly advantageous for metrology and communication systems, especially in scenarios where long-term frequency stability is not a paramount requirement. For further performance improvement, temperature fluctuations can be mitigated by sealing the fiber in a temperature-stabilized enclosure[4], and mechanical vibration can be suppressed by using a vibration-insensitive optical fiber spool[5]. Furthermore, a fully on-chip integrated solution would also mitigate this problem to a certain extent.

To further analyze the relationship between the SIL&OIL frequency noise and the TRN limit, we additionally compared it with the TRN of the extended fiber cavity and the 1 GHz microresonator according to Equations (7) and (8) in the main text, as shown in Supplementary Figure 9. For the calculation parameters of the fiber cavity, cavity geometries: $R = 37/2\pi$ m. The material parameters for the fiber core were as follows: density, $\rho = 2.20 \times 10^3$ kg m^{-3}; thermal conductivity, $\kappa = 1.38$ W m^{-1}K^{-1}; specific heat capacity, $C = 740$ J kg^{-1} K^{-1}; environmental temperature, $T = 298$ K; fundamental mode halfwidths, $d_z = 3.5$ μm and $d_r = 0.8$ μm, with orbital number l, azimuthal number m and meridional number $p = l - m = 0$.

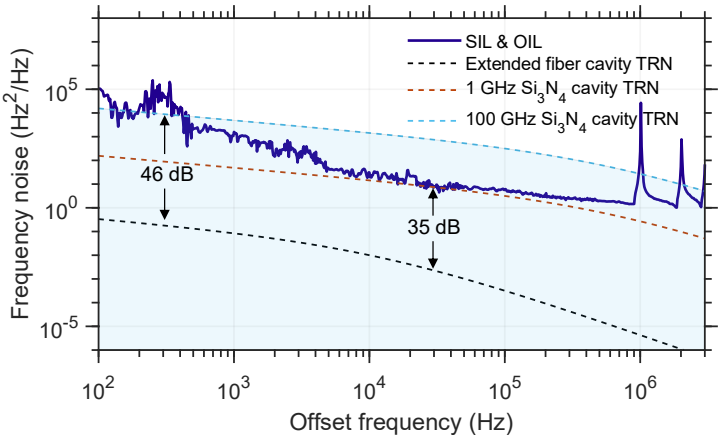

Supplementary Figure 9. Frequency noise comparison with TRN limits. The SIL&OIL comb noise (dark blue) surpasses the TRN limit of the 100-GHz microresonator (blue dash) and approaches that of a 1-GHz resonator (brown dash). The TRN of the extended fiber cavity is also provided for comparison (black dash).

As shown in Supplementary Figure 9, the TRN-induced frequency noise of the fiber cavity is approximately 46 dB lower than that of the 100-GHz microresonator, owing to its much larger mode volume (~0.7×10^6 times larger). Furthermore, this TRN limitation is more than 35 dB lower than the experimentally measured SIL&OIL frequency noise spectrum, confirming that the extended cavity's TRN is not the dominant factor limiting the SIL&OIL linewidth.

Instead, the achievable linewidth is constrained by the effective photon lifetime in the feedback cavity, which according to Eq. (2) in the main text depends on the round-trip delay τ_f and the feedback ratio η. In principle, increasing τ_f (longer fiber) or η could further reduce noise, but practical limitations arise. Longer fibers introduce greater sensitivity to environmental perturbations (e.g. temperature, vibration), reducing the maximum stable η. Moreover, too large η leads to soliton coherence collapse (regime ③ in Fig. 4). These factors restrict the effective photon lifetime extension and thus the attainable linewidth. By comparison, the frequency noise level achieved in our system approaches that of a 1-GHz resonator, as shown in Supplementary Figure 9, demonstrating that we have effectively overcome the TRN limit of the original high-FSR microresonator, even though we have not yet reached the fundamental TRN floor of the extended fiber cavity.

Supplementary Note 6. Single-soliton microcomb linewidth results

Supplementary Figure 10 shows the integral linewidth of the comb modes from -20 to 20 (relative to the pump line) for the single-soliton state before and after pump-OIL, measured at a low feedback ratio of $\eta = 0.025$. At this relatively low feedback power, which ensures stable single-soliton operation, all comb modes exhibit a narrowed integral linewidth of approximately 4 kHz. This value is about one-ninth of the linewidth in the SIL-only state and, importantly, reaches the thermo-refractive noise (TRN) limit of the 100-GHz microresonator. This result demonstrates that even with minimal OIL feedback, our system can achieve coherence at the fundamental noise floor set by the cavity.

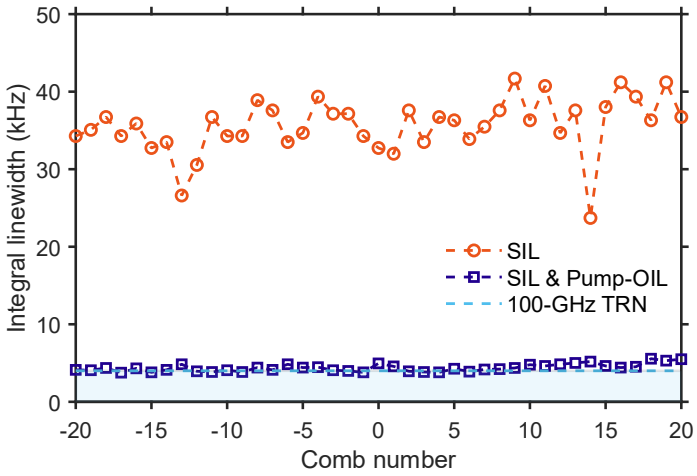

Supplementary Figure 10. Integral linewidth of comb lines in the single-soliton state. With pump-OIL at η = 0.025, all comb modes from –20 to +20 exhibit a narrowed linewidth of ~4 kHz, reaching the TRN limit (blue dash) of the 100-GHz resonator.

Supplementary Note 7. Repetition-rate phase noise under SIL&OIL

To investigate whether the dramatic linewidth reduction achieved via Pump-OIL translates into improved repetition rate stability, we characterized the phase noise of the microcomb's repetition rate under both SIL-only and SIL&Pump-OIL conditions. Since the 100.7 GHz repetition rate cannot be directly measured using a PD and a phase noise analyser, we employ a down-conversion method. The complete experimental set-up is presented in Supplementary Figure 11a. We tap a portion of the cascaded injection locking microcomb going through an electro-optic modulator (EOM) driven at 20 GHz to generate an electro-optic comb. Then a TBPF selects two phase-modulated comb teeth whose beat note (~706 MHz) is amplified and detected using a photodiode and processed with a phase noise analyzer (PNA).

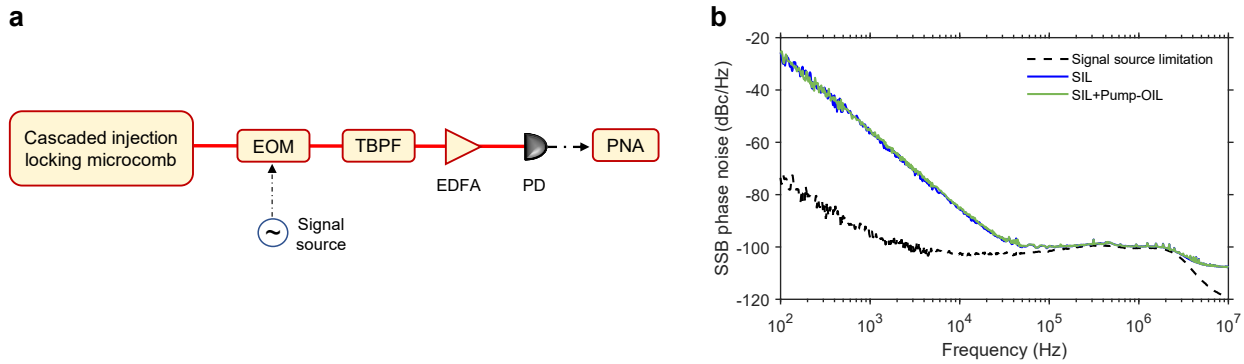

Supplementary Figure 11. Phase noise characterization of cascaded injection locking microcomb. a, Complete experimental setup. EOM: Electro-optical modulator; TBPF: Tunable band-pass filter; EDFA: Erbium-doped fiber amplifier; PD: Photodetector; PNA: Phase noise analyser. **b**, SSB phase noise of down converted repetition rate of the SIL and SIL+Pump-OIL microcomb. The signal source limitation is also listed as reference.

Supplementary Figure 11b presents the single-sideband (SSB) phase noise of the down-converted repetition rate for both the SIL-only and SIL+Pump-OIL microcombs. Both conditions present nearly identical phase noise level. This result clearly shows that although the pump laser's frequency noise is reduced (from 31 Hz to 3.1 Hz Lorentzian linewidth), the repetition-rate phase noise remains unchanged. Such apparent discrepancy can be understood by examining the distinct mechanisms that govern pump frequency noise and repetition rate noise.

Firstly, for pump frequency noise. The external fiber delay line extends the effective pump photon lifetime and creates a composite cavity system that combines the microresonator and the fiber loop. For the pump laser, the effective reference for frequency stabilization becomes this composite cavity, rather than the microresonator alone. By locking to this composite cavity, the pump laser experiences a diluted noise floor, enabling its frequency noise to fall below the intrinsic TRN limit of the original microresonator (Fig. 2d in the main text). This explains the observed pump linewidth reduction.

Then, for the repetition rate noise. The repetition rate f_{rep} of a dissipative Kerr soliton microcomb is determined by $f_{\mathrm{rep}} = D_1 + \frac{D_2}{D_1}\Omega(\delta\omega) + \cdots$, where D_1 is the free spectral range (FSR), D_2 is the

group velocity dispersion, and $\Omega(\delta\omega)$ represents frequency shifts (e.g., Raman self-frequency shift) that depend on the pump-cavity detuning $\delta\omega$. Importantly, D_1 and D_2 are intrinsic parameters of the microresonator, directly affected by its material properties and thermal fluctuations. These parameters experience the same TRN as the original microresonator, and they are not diluted by the external feedback loop because the loop does not alter the cavity's physical properties or its thermal environment.

Although the Pump-OIL scheme may suppress fluctuations in the detuning $\delta\omega$, the remaining fluctuations in D_1 and D_2, which arise from the microresonator's own TRN, continue to contribute directly to the repetition rate noise. Furthermore, other mechanisms such as quantum timing jitter[6] and relative intensity noise (RIN)[7] can also contribute to repetition rate fluctuations and are not mitigated by pump frequency noise reduction. Thus, while the pump laser's frequency noise is diluted by the composite cavity, the intrinsic noise of the microresonator's modal parameters remains undiluted and dominates the repetition rate phase noise. This explains why the repetition rate stability is unchanged despite the dramatic improvement in pump linewidth.

We also note that in Supplementary Ref. 8, repetition rate phase noise reduction is observed when sideband OIL is implemented. In that configuration, an external fixed-frequency fiber laser was used as the pump, and a sideband comb line was filtered and reinjected. The resulting dual-pinning of both the pump and the locked sideband stabilized the repetition rate, leading to observable phase noise improvement. Our cascaded SIL&Pump-OIL architecture differs fundamentally from Supplementary Ref. 8. The pump laser is already SIL-locked to the microresonator before OIL is applied. Consequently, the pump frequency is slaved to the cavity mode, and no independent external frequency reference exists. Thus, our cascaded injection locking architecture does not realize the dual-pinning function, resulting in no change in the repetition-rate phase noise.

Supplementary Note 8. Soliton dynamics and frequency noise of sideband line under SIL&Pump-OIL

To verify that the coherence improvement under Pump-OIL extends uniformly to all comb lines, we performed a detailed self-heterodyne characterization of a representative sideband comb line (μ = +16) under the same cascaded SIL&Pump-OIL configuration, and systematically analyzed the evolution of its noise dynamics and frequency noise under different feedback ratio η. As shown in Supplementary Figure 12a, the sideband comb establishes three dynamical regimes identical to those of the pump line, with approximately the same feedback ratios for the corresponding regimes.

In addition, the evolution of the frequency noise spectrum in Supplementary Figure 12b shows the same trend of narrowing first and then broadening. The integral linewidth decreases monotonically from 35 kHz (SIL state) to an optimum of 1.3 kHz until the onset of coherence collapse, beyond which it degrades abruptly. All the above experiments demonstrate that under

SIL&Pump-OIL, the sideband comb line exhibit the same dynamical and linewidth behaviors as the pump line.

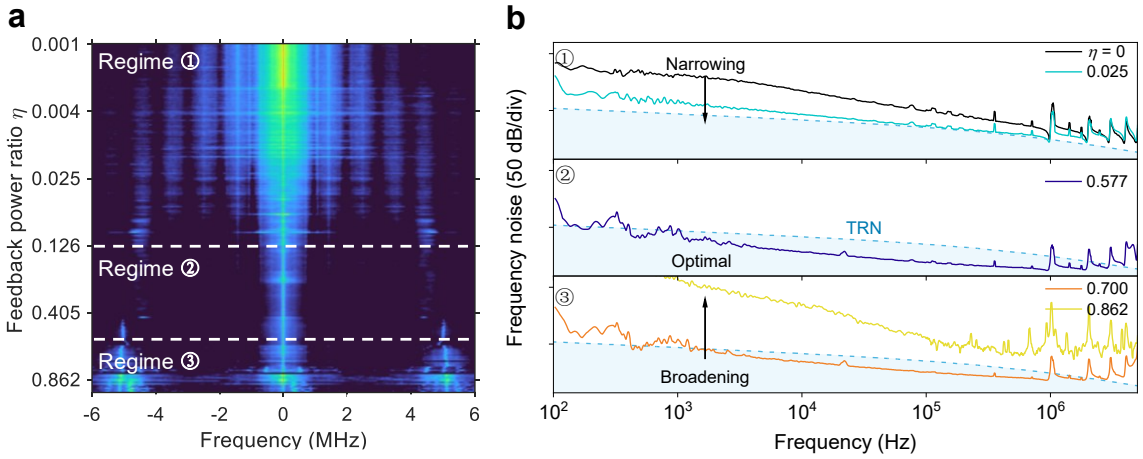

Supplementary Figure 12. Soliton dynamics and frequency noise evolution versus feedback ratio of sideband comb (μ = +16) under cascaded SIL&Pump-OIL conditions. a, Evolution of the sideband line's delayed self-heterodyne spectra. **b,** Evolution of the measured frequency noise. The blue dashed line indicates the resonator's TRN limit.

Supplementary Note 9. Microcomb soliton dynamics under sideband optical-injection locking (SB-OIL)

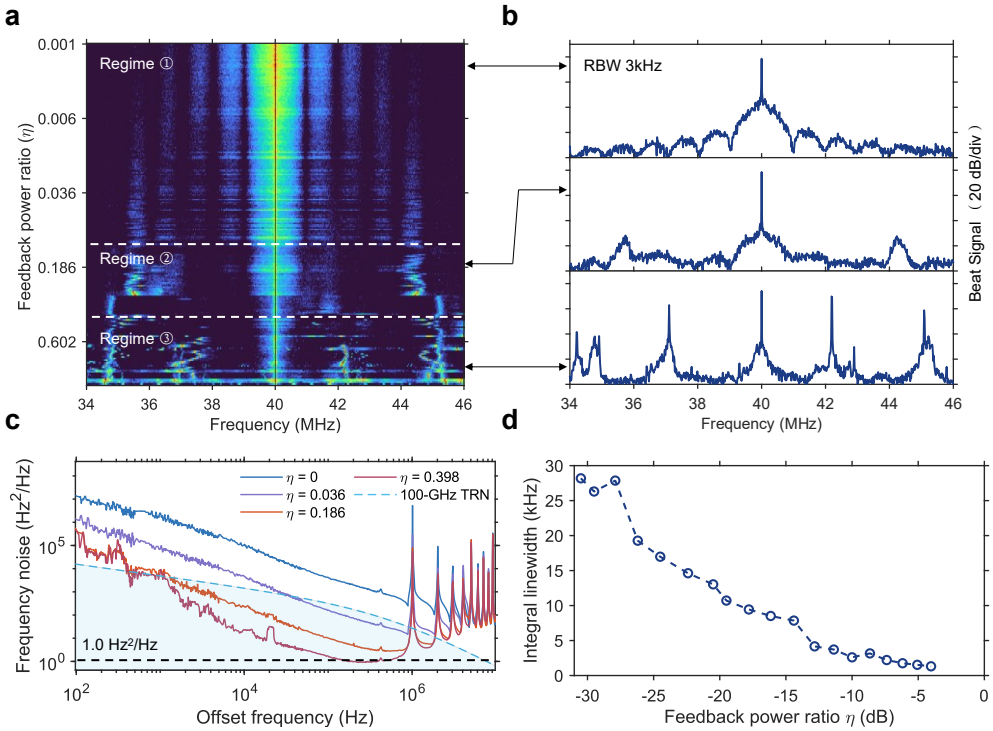

Supplementary Figure 13. Microcomb soliton dynamics of cascaded SIL&sideband-OIL. a, Evolution of delayed self-heterodyne spectra with increasing feedback power ratio η. **b,** Representative beating spectra in three dynamical regimes. **c,** Frequency noise evolution with η. **d,** Integral linewidth as a function of η.

SB-OIL exhibits dynamics with three distinct regimes (Supplementary Figure 13a, b, lock to mode μ = +16), similar to pump-OIL. However, in regime ②, the oscillator frequency exhibits noticeable drift due to the weak intracavity power of the sideband comb line, making it more susceptible to environmental perturbations such as temperature fluctuations and fiber vibration.

Supplementary Figure 13c and d show the evolution of the measured frequency noise and the corresponding integral linewidth as the feedback ratio η increases within regimes ① and ②. Both the frequency noise and integral linewidth show a continuous decreasing trend. The white frequency noise floor can be suppressed to 1 Hz^2/Hz—a level equivalent to the best performance achieved with pump-OIL.

Supplementary Note 10. Loss estimation of fully integrated architecture

According to the proposed simplified on-chip integrated SIL&Pump-OIL architecture in Fig. 5b in the main text, it includes several key devices: a thick Si_3N_4 Vernier filter, a thin Si_3N_4 spiral delay, and two adiabatic tapers connecting the thick and thin Si_3N_4 layers.

(a) Thick Si_3N_4 Vernier filter

Supplementary Ref. 9 provides the detailed design parameters of the Vernier filter. The microcavity has a thickness of 700 nm and a width of 2.1 μm, with a minimum coupling gap of 0.3 μm between the bus waveguide and the microcavity. Simulations show a filtering insertion loss of −1.6 dB at the on-resonance frequency, corresponding to a single-pass insertion loss of −3.2 dB for the Vernier filter.

(b) Thin Si_3N_4 spiral delay

Supplementary Ref. 10 presents the design parameters of the thin Si_3N_4 spiral delay line. The waveguide dimension is 6 μm × 80 nm, with a total length of 10 m. Given a waveguide propagation loss of 0.2 dB/m, the total delay loss is estimated to be approximately −2 dB.

(c) Adiabatic tapers

The purpose of adiabatic tapers is to achieve low-loss optical field transfer between the thick Si_3N_4 and thin Si_3N_4 layers. Supplementary Ref. 11 provides the detailed design parameters: the thick waveguide is gradually tapered down to 200 nm, while the thin Si_3N_4 waveguide width is gradually widened from 200 nm. The taper propagation length is 1 cm. This architecture can achieve a loss of below 0.1 dB, and the total loss for two adiabatic tapers is estimated to be −0.2 dB.

The total loss of the above key devices is estimated to be −5.4 dB (η = 0.288), which still falls within the moderate feedback regime ② (0.126 < η < 0.577, optimal linewidth) for feedback. This enables efficient OIL and noise suppression. Therefore, the proposed full on-chip design represents a feasible fully integrated solution.

Supplementary Note 11. Numerical modeling of the SIL & OIL microcomb

The dynamics of the microcomb under SIL and OIL are modeled using a dimensionless form of the Lugiato–Lefever equation (LLE) that incorporates optical injection and backscattering[12]:

$$\left(\frac{\partial}{\partial\tau}E_{\mathrm{F}} = \left(-1 - i\Delta + i\frac{\beta_2}{2}\frac{\partial^2}{\partial\theta^2} + i|E_{\mathrm{F}}|^2 + 2i\overline{|E_{\mathrm{b}}|^2}\right)E_{\mathrm{F}} + ig_{\mathrm{b}}\overline{E_{\mathrm{b}}} + F\right) \quad \text{(S7)}$$

here, E_{F} is the normalized intra-cavity field in the forward direction, E_{b} is the back-scattered field, $\tau = \kappa t/2$ denotes the normalized time, with κ being the total cavity decay rate, $\Delta = 2\delta\omega/\kappa$ is the normalized laser-cavity detuning, $\beta_2 = 2D_2/\kappa$ is the normalized second-order dispersion parameter, θ is the azimuthal coordinate, and g_b is normalized backscattering parameter.

To model the optical feedback from the external loop, a feedback field is added to the input field. The normalized pumping strength $F(\theta, t)$ is extended as:

$$F = F_p + F_b e^{i\mu\theta} \quad \text{(S8)}$$

where $F_p = \sqrt{P_{\mathrm{in}}/P_{\mathrm{th}}}$ is the normalized pump amplitude, P_{in} is the pump power and P_{th} is the parametric threshold power, $F_b = \sqrt{\left(S_{in}()^2{}_0 e^{-i\varphi}{}_{\mathrm{th}}\right)}$is the normalized feedback amplitude. Here, $S_{\mathrm{in}}^2 = \left(\frac{E_F\sqrt{\frac{\kappa}{2g}}\left(\frac{\kappa}{2}+i\delta\omega\right)}{\sqrt{\kappa_{\mathrm{ex}}}}\right)^2$ is the calculated photon flux of the OIL-targeted comb line (mode index μ, where $\mu = 0$ corresponds to the pump and $\mu \neq 0$ to a sideband), g is the per photon Kerr Shift, η represents the feedback power ratio, φ represents the phase delay of the feedback loop. In the simulation, the feedback loop length was set to be 37 m.

The back-scattered field E_{b} is also described by the same equation:

$$\left(\frac{\partial}{\partial\tau}E_{\mathrm{b}} = \left(-1 - i\Delta + i\frac{\beta_2}{2}\frac{\partial^2}{\partial\theta^2} + i|E_{\mathrm{b}}|^2 + 2i\overline{|E_{\mathrm{F}}|^2}\right)E_{\mathrm{b}} + ig_{\mathrm{b}}\overline{E_{\mathrm{F}}}\right) \quad \text{(S9)}$$

In addition, the laser-cavity detuning Δ under SIL is described by

$$\Delta = \Delta_{\mathrm{L}} + K\,Im\left[e^{i\phi}\frac{\overline{E_{\mathrm{b}}}}{F}\right] \quad \text{(S10)}$$

where Δ_{L} is the normalized laser-cavity detuning without the feedback, K is the feedback strength, and ϕ is the feedback phase.

In the simulations presented in Fig. 4c in the main text, the following parameters were used: $P_{\mathrm{in}} \approx 7.5$ mW ($F_p \approx \sqrt{4.5}$), $D_2/2\pi = 0.36$ MHz, K = 40, and g_{b} = 0.5. Parameters not directly measurable in experiments, such as Δ_{L} and ϕ, were adjusted to match the experimental behavior.

For the frequency noise simulations, we follow the scheme described in the Supplementary Ref. 8. The pump phase noise is included into pump F_p by assigning it a time-dependent phase φ_{n} as $F_p' = F_p \times e^{i\varphi_n}$, and

$$\varphi_n = \sqrt{2\pi\Delta\upsilon_p/FSR} \times \xi \quad \text{(S11)}$$

where $\Delta\upsilon_p = 30$ Hz and ξ stands for the intrinsic linewidth of the pump and a normally distributed random number, respectively.

The simulation is first initialized without feedback to obtain a stable soliton microcomb state. The feedback field is then stored in a memory buffer and reused after the round-trip time of the feedback cavity to account for the optical injection-locking effect. To achieve a stationary description of the laser with optical feedback, the program is run for an additional 5.12 million roundtrips. The phase of the selected mode for OIL is recorded every 258 roundtrips, and the frequency noise PSD is computed based on the recorded phase sequence.

Supplementary Figure 14 illustrates the detailed temporal evolution of the intracavity power distribution for representative feedback ratios η = 0.05, 0.32, and 0.71. The feedback is activated at $\tau = 20$, triggering the transition from an initial single-soliton state into distinct dynamical regimes: a stable single-soliton, a perturbed multi-soliton state, and fully chaotic dynamics.

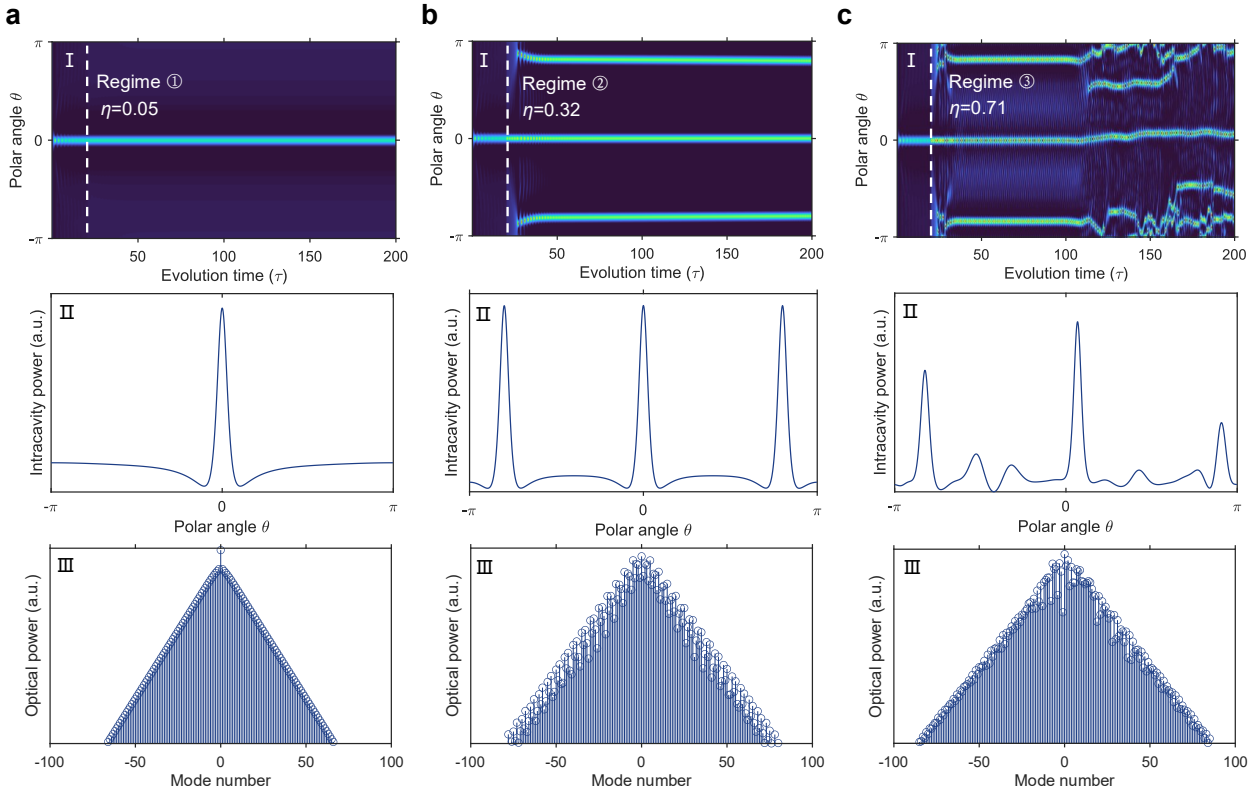

Supplementary Figure 14. Numerical simulation of microcomb soliton dynamics under OIL. Intracavity power evolution for feedback ratios η = 0.05 **a,** 0.32 **b** and 0.71 **c**, showing transitions from single-soliton (①), through disturbed multi-soliton (②), to chaotic dynamics (③). Top: spatiotemporal power. Middle: field snapshot at τ = 200. Bottom: steady-state optical spectrum at τ = 200.

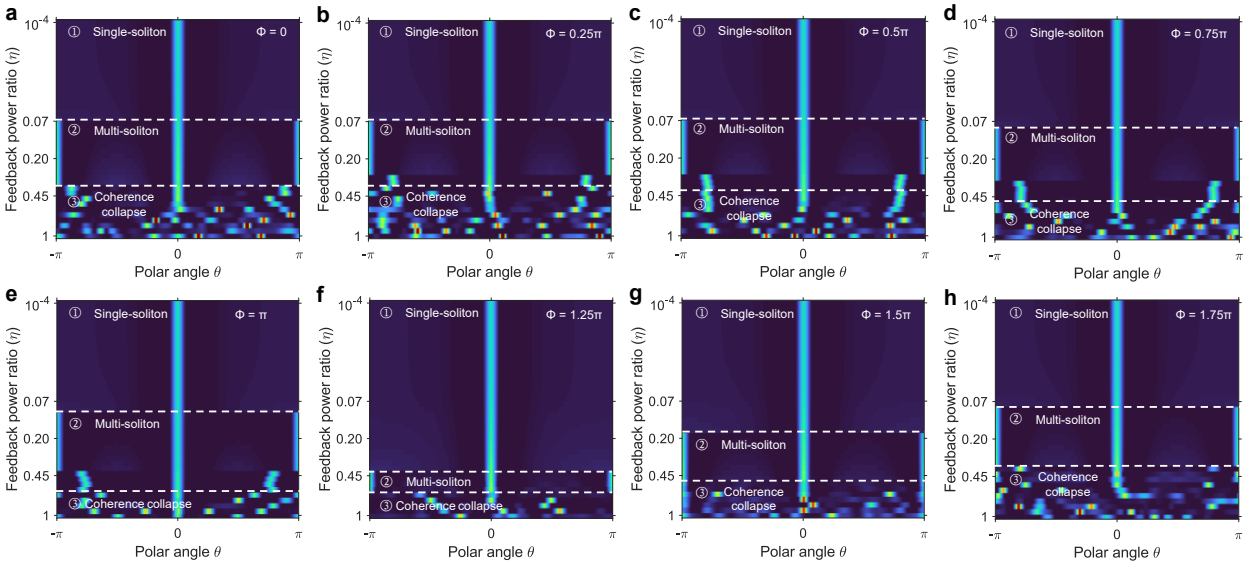

Supplementary Figure 15. Numerical simulation of soliton dynamics versus η under different feedback phase. a–h correspond to feedback phases Φ = 0, 0.25π, 0.5π, 0.75π, π, 1.25π, 1.5π and 1.75π, respectively.

In addition, we performed numerical simulations to analyze the soliton evolution dynamics by varying the phase of the feedback light. As shown in Supplementary Figure 15, panels a–h correspond to feedback phases Φ = 0, 0.25π, 0.5π, 0.75π, π, 1.25π, 1.5π and 1.75π, respectively. It can be observed that Φ indeed influences the boundaries between different dynamical regimes (single-soliton, multi-soliton, and coherence collapse). Supplementary Figure 16 summarizes the regime distribution of soliton dynamics under different feedback phases. At Φ = 1.25π, the single-soliton region is the largest and the coherence collapse threshold reaches $\eta \approx 0.63$, the highest among all phases. At other phases, this threshold can be as low as $\eta \approx 0.35$.

It should be noted, however, that the simulation results above are obtained under ideal conditions without environmental perturbations. In the experiments, the feedback phase is subject to continuous fluctuations due to temperature drift, mechanical vibrations of the fiber, and frequency jitter of the pump laser. If the system is highly phase-sensitive, we would expect to observe switching or flickering between single-soliton, multi-soliton, and coherence collapse states, as the phase varies over time. However, no such behavior was observed in our measurements. One possible explanation is that rapid and random phase fluctuations average out any phase-dependent effects over the measurement time, making the dynamics appear phase-insensitive. However, the underlying mechanism is not fully understood and warrants further investigation.

Despite the theoretical phase dependence observed in simulations, our combined experimental and simulation results allow us to identify a practical operating regime where stable performance is guaranteed. As shown in Supplementary Figure 16, for $\eta < 0.35$, the system remains free from coherence collapse under all feedback phases. This means that even with uncontrolled phase fluctuations in a real experiment, reliable optical injection locking and noise suppression can be achieved, as long as the feedback ratio stays below this threshold.

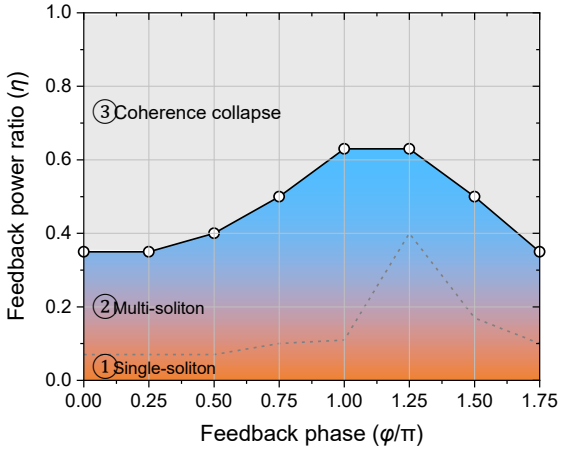

Supplementary Figure 16. Regime distribution of soliton dynamics under different feedback phases from 0 ~ 1.75π.

For the fully on-chip integrated design discussed in Supplementary Note 10, the estimated total loss is −5.4 dB, corresponding to $\eta \approx 0.288$. This value falls well within the safe regime ($\eta < 0.35$), indicating that phase sensitivity does not pose a fundamental obstacle to integration. Stable OIL operation and effective noise suppression can therefore be expected in practical on-chip devices.

Next, we further analyzed the soliton evolution dynamics under SB-OIL. As shown in Supplementary Figure 17a, the soliton dynamics under sideband-OIL is slightly different from that of Pump OIL shown in Fig. 4c in the main text. In the single-soliton regime, the soliton pulse remains stable but exhibits a central pulse drift. This is because the increased power of the injected sideband effectively modifies the time-domain background inside the microcavity, resulting in a shift of the soliton's central position[13]. As the feedback ratio increases, this drift leads to a more random distribution of multi-soliton states. This random multi-soliton state explains the disappearance of the sech^2 spectral profile observed in Fig. 3 in the main text. Moreover, the simulations show that sideband-OIL enters the coherence collapse regime at a lower feedback ratio of $\eta \approx 0.17$, a value much lower than the pump-OIL ($\eta \approx 0.35$ accounting the phase sensitivity). This confirms that the soliton dynamics become more fragile under sideband injection, which is consistent with the experimental findings in Fig. 3 in the main text.

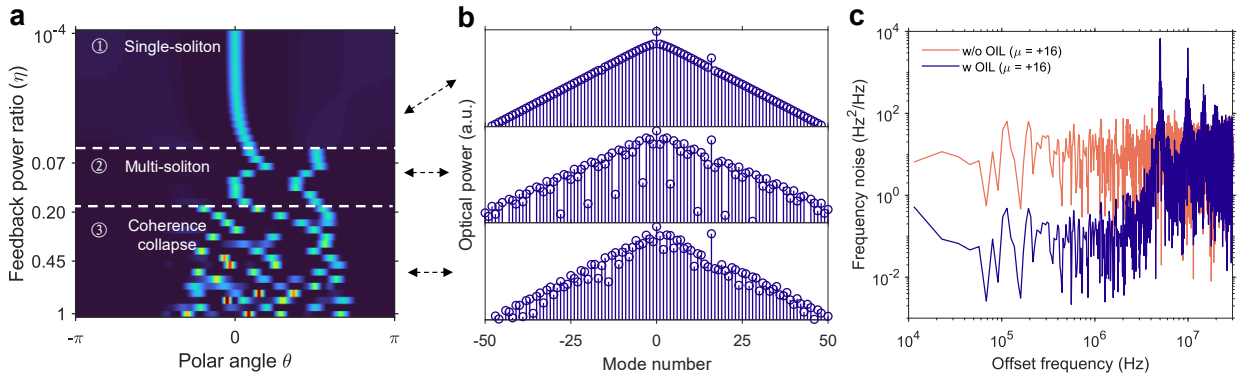

Supplementary Figure 17. Numerical study of SB-OIL of the soliton microcomb. a, Numerical simulation of intracavity field evolution versus η. b, Representative optical spectra in the three different feedback regimes. c, Comparation of frequency noise results of the mode +16 without or with OIL.

Supplementary Figure 17b shows the representative comb spectra in the three different feedback regimes. The simulated multi-soliton spectrum in the middle corresponding to that of Figure 3b in the experiment, which also shows an irregular comb spectrum. Supplementary Figure 17c, we present the frequency noise results of mode +16 before and after OIL. Without OIL, the frequency noise is modeled as a flat power spectral density corresponding to white noise, with an intrinsic linewidth of approximately 30 Hz. After SB-OIL, consistent with the experimental results in Figure 3, significant noise suppression is achieved: the frequency noise is reduced by two orders of magnitude in the low-offset frequency region. This confirms that noise dilution is realized through the time-delay feedback feedback link. Characteristic noise spikes near 5 MHz induced by optical feedback (~37 m in this work) are also clearly observed, verifying that our numerical simulation well captures the key dynamical features under OIL.

Supplementary References:

1. Kondratiev, N. M. et al. Recent advances in laser self-injection locking to high-Q microresonators. *Frontiers of Physics* **18**, 21305 (2023).
2. Kondratiev, N. M. et al. Self-injection locking of a laser diode to a high-Q WGM microresonator. *Opt. Express* **25**, 28167 (2017).
3. Ye, Z. et al. Foundry manufacturing of tight-confinement, dispersion-engineered, ultralow-loss silicon nitride photonic integrated circuits. *Photonics Res.* **11**, 558-568 (2023).
4. Tetsumoto, T. et al. Optically referenced 300 GHz millimetre-wave oscillator. *Nat. Photon.* **15**, 516-522 (2021).
5. Jeon, I. et al. Palm-sized, vibration-insensitive, and vacuum-free all-fiber-photonic module for 10-14-level stabilization of CW lasers and frequency combs. *APL Photonics* **8**, 120804 (2023).
6. Yao, L. et al. Soliton microwave oscillators using oversized billion Q optical microresonators. *Optica* **9**, 561-564 (2022).
7. Aldhafeeri, A. et al. Low phase noise K-band signal generation using polarization diverse

single-soliton integrated microcombs. *Photonics Res.* **12**, 1175-1185 (2024).
8. Lei, F. et al. Self-injection-locked optical parametric oscillator based on microcombs. *Optica* **11**, 420 (2024).
9. Liu, Y. et al. A fully hybrid integrated erbium-based laser. *Nat. Photon.* **18**, 829–835 (2024).
10. Heim, D. A. S. et al. Hybrid integrated ultra-low linewidth coil stabilized isolator-free widely tunable external cavity laser. *Nat. Commun.* **16**, 5944 (2025).
11. Xiang, C. et al. 3D integration enables ultralow-noise isolator-free lasers in silicon photonics. *Nature* **620**, 78-85 (2023).
12. Ji, Q.-X. et al. Engineered zero-dispersion microcombs using CMOS-ready photonics. *Optica* **10**, 279-285 (2023).
13. Wildi, T. et al. Sideband injection locking in microresonator frequency combs. *APL Photonics* **8**, 120801 (2023).